INTERNATIONAL JOURNAL FOR NUMERICAL METHODS IN FLUIDS
Int. J. Numer. Meth. Fluids 2008; **57**:877–903
Published online 13 November 2007 in Wiley InterScience (www.interscience.wiley.com). DOI: 10.1002/fld.1657

Wavelet-based adaptive grids as applied to hydrodynamics

C. W. Smith[1,*,†], J. Zang[2] and R. Eatock Taylor[1]

[1]*Department of Engineering Science, University of Oxford Parks Road, Oxford OX1 3PJ, U.K.*
[2]*Department of Architecture and Civil Engineering, University of Bath, Bath BA2 7AY, U.K.*

SUMMARY

An adaptive, wavelet-based, multiscale finite-volume scheme is developed and employed to investigate applications in the simulation of water waves. Firstly, two one-dimensional, strictly hyperbolic cases are investigated: shallow water and Euler equations. These are followed by two investigations using a finite-volume formulation of Madsen and Sørensen's Boussinesq equations. Converged results were obtained in all cases, which demonstrate that the adaptive grid scheme is significantly faster than that on a uniform grid. In some cases, one-seventh of the number of cells is required to obtain the same accuracy as that of the uniform grid. Issues of stability are discussed in the context of the particular problems modelled here with the Boussinesq equations, related to discretization of the high-order spatial derivatives on a non-uniform grid. Copyright © 2007 John Wiley & Sons, Ltd.

Received 20 March 2007; Revised 21 September 2007; Accepted 2 October 2007

KEY WORDS: finite-volume methods; hydrodynamics; mesh adaptation; adaptivity; free surface; shallow water; Boussinesq

1. INTRODUCTION

Many problems are encountered in engineering where fluid flow with a free surface is an important feature. These include wave loading and run-up on coastal and offshore structures such as breakwaters and offshore platforms; on land, fluvial problems and land-based hydraulic structures; bubbly and multi-phase flow in pipes; groundwater flow. These problems are often difficult to solve as the position of the free surface is not known in advance and must be determined as the simulation proceeds.

Free-surface flow and in particular the behaviour of surface waves has been studied for many years [1] and a variety of numerical methods have been developed. Numerical methods based on

*Correspondence to: C. W. Smith, Department of Engineering Science, University of Oxford, Parks Road, Oxford OX1 3PJ, U.K.
†E-mail: christopher.smith@eng.ox.ac.uk

Contract/grant sponsor: EPSRC

linear wave theory using potential flow have a long history and have found considerable use in industry. However, linear wave theory assumes an infinitesimal wave height and correspondingly small particle velocities. For engineering design purposes, the most important environmental cases are those featuring large, steep, non-linear waves, for which the linear theory is inapplicable. One approach to account for the non-linearity is to perform a Stokes perturbation expansion and separate the wave into first-, second- and higher-order terms. An alternative approach is to assume that the waves are fully non-linear. The fluid can then be modelled either by using a velocity potential in an interface-tracking method or by solving the Euler and Navier–Stokes equations. This paper is directed towards development of the methodology for solving the Euler equations using a finite-volume scheme on a wavelet-based adaptive grid.

Adaptive grids are useful in fluid dynamics as problems typically exhibit a wide variety of spatial scales. The solution may vary rapidly in some regions and slowly in others. The accuracy of a computational scheme depends on a discretization at a resolution high enough to represent the detailed features of the solution. Under such conditions, a uniform fine discretization is impractical and inefficient. It is computationally more effective to employ an adaptive grid so that maximal accuracy is obtained in the regions varying most rapidly through use of smaller-sized cells, while in the regions where the solution varies more slowly, larger cells can be used. An arbitrary accuracy can thus be obtained for a lower computational work load than for a uniform discretization.

Wavelets, traditionally used in applications such as signal processing and image compression, have become an important tool in numerical computation. Cohen *et al.* [2] and Dahmen [3, 4] give recent overviews of their applications. Since wavelets are series of scaled and dilated basis functions, they can represent functions at different levels of resolution and hence can be used to define an adaptive grid. Just as with modern image compression techniques, detail below a certain threshold can be discarded so that the storage requirement is reduced. As fewer cells or elements are required, the computational burden for the solution method is also reduced. There has been a great deal of work in the area of such adaptive methods, originally with a particular emphasis on elliptical equations. As Dahlke *et al.* [5] suggest, it is with adaptivity that the most immediate potential benefit can be found with regard to wavelet discretizations.

An application of wavelet-based discretizations in modelling continuum problems is the multi-scale finite-volume method (finite/boundary element and finite difference applications also exist: Wavelet-Galerkin, see e.g. Amaratunga *et al.* [6] and wavelet collocation methods, Bertoluzza [7]). Multiscale finite-volume schemes were first reported by Harten [8, 9]. The numerical solution is expressed as a multiresolution representation comprising a coarse mesh and wavelet coefficients on a series of nested grids. Wavelet coefficients were shown in [9] to indicate the local smoothness of the solution, thus acting as an error indicator. The scheme is faster than a given finite-volume scheme on a uniform fine mesh, as the flux is only evaluated on the finest grid in regions of high gradient; elsewhere it is approximated at coarser scales. A two-dimensional implementation was produced by Bihari and Harten [10]. While this particular method accelerates a given finite-volume scheme, Cohen *et al.* [11] note that it is not truly adaptive. The speed gain is limited by the fact that the evolution stage, where the solution is updated at the next time step as determined by the difference scheme, takes place on the finest grid level. The solution is not computed in a compressed form and so the computation time and storage requirements remain proportional to the size of the uniform grid at the finest level.

Cohen *et al.* [11] go on to describe a fully adaptive scheme where the computational cost of a time step and the memory storage requirement are both proportional to the number of wavelet coefficients used to describe the solution, providing an error analysis for the scheme. Cohen

DOI: 10.1002/fld

et al. [12], by constructing a multiresolution scheme using triangles, have also shown that it is not necessary to perform the computation on a cartesian grid. Bramkamp *et al.* [13] used parametric meshes to map grid cells to splines enabling them to discretize the fluid surrounding an aerofoil. The scheme has also been implemented to model cavitation and shock–bubble interactions by Andreae *et al.* [14]. Müller [15] presents an adaptive multiscale scheme in great detail and describes an implementation, reporting good performance.

Another commonly used way to incorporate grid adaptivity is through adaptive quadtree grids, such as used by Greaves and Borthwick [16], Ham *et al.* [17] and Wang *et al.* [18]. These partition the domain in a hierarchical grid, storing the cell data in a tree-based structure. While the resulting grids appear similar to those obtained through adaptive multiscale schemes, it will be seen in Section 2 that the use of the multiscale wavelet transform means that the process of generating the grids is very different, working with the multiscale wavelet transform of the data. The difference is to some degree analogous to working in the wave number rather than the spatial domain using the Fourier transform; while both representations are equivalent, it will be seen that there are particular advantages to working on the transformed data.

In considering the application of such a multiscale method to hydrodynamics, a major step is to demonstrate its viability in one dimension. This paper describes how a scheme based on Müller's work [15] has been implemented for the solution of various computational problems with a view to extending it to free-surface flow modelling in two and three dimensions. Two strictly hyperbolic cases are first investigated: the dam-break problem using the shallow water equations, and the interacting blast-wave problem of Colella and Woodward [19]. The solutions to these two problems feature prominent shock waves as well as smooth regions and as such are well suited to an adaptive grid approach. Two further cases are then investigated in one dimension: solitary-wave reflection from a wall and propagation over a steep step. The latter cases are modelled using a formulation of the Boussinesq equations that features a hyperbolic stage followed by an elliptic stage. In many previous finite-volume solutions to the Boussinesq equations a uniform grid has been used. This is because, despite the strong localization of solitary-wave solutions, the high-order derivatives make non-uniform-grid calculations difficult; larger computational stencils must be used, which can be difficult to formulate and increase the bandwidth of the resulting system of equations. The incompressible Euler equations will be solved in two dimensions in the next stage of work. The objective of the present studies is to investigate some of the issues that could arise in extending the described approach to the modelling of a wide class of free-surface flow problems in two and three dimensions, based on solving the incompressible Euler equations. In such a model, when one wishes to ensure pressure–velocity coupling, an approach such as the SIMPLE algorithm must be used, involving the solution of an elliptic equation. One of the contributions of this article, therefore, is to explore the viability of elliptic corrections using the multiscale finite-volume scheme, originally derived for hyperbolic conservation-laws.

The multiscale finite-volume scheme is described in Section 2 and results for the four test cases are presented in Section 3. Section 4 presents some conclusions and some implications for future work.

2. MULTISCALE FINITE-VOLUME SCHEME

In this scheme the grid, upon which the finite-volume flux calculations are performed, is adapted at each time step using criteria from a wavelet-transformed representation of the solution. The process

DOI: 10.1002/fld

can be divided into five stages, which are explored in more detail in the following subsections. These are: the multiscale transform; thresholding of details; prediction of the grid at the next time step; inverse multiscale transform; calculation of the fluxes and time integration.

2.1. The multiscale transform

The multiscale transform described in this section is first introduced for a general function $q(x)$ defined along the axis Ox, where x is suitably non-dimensionalized. It is later applied to the system of conservation laws, in effect the values of the conserved variables at a particular time step. The function is decomposed into wavelet bases, leading to a low resolution, coarse approximation and a succession of 'details' at increasingly finer levels. These details represent the local deviation from the coarse scale average. It will be seen below that these wavelets possess several properties that make it useful to perform such a decomposition.

We can consider the one-dimensional domain $[0, 1]$, over which there is a hierarchical series of nested grids, each created from uniform dyadic partitioning of the previous grid. Introducing j to denote the partitioning level, it is clear that on a such dyadic grid there are 2^j cells. Thus each cell, $V_{j,k}$, where $k=0,\ldots,2^j-1$, is of size $|V_{j,k}|=2^{-j}$. On these grids, the box function can be introduced:

$$\tilde{\phi}_{j,k}(x)=\begin{cases}|V_{j,k}|^{-1}, & x\in V_{j,k}\\ 0, & x\notin V_{j,k}\end{cases} \tag{1}$$

$$=\begin{cases}2^j, & x\in 2^{-j}[k,k+1]\\ 0, & x\notin 2^{-j}[k,k+1]\end{cases} \tag{2}$$

The box function is L^1-normalized with respect to $[0, 1]$. The tilde is present to distinguish between these functions and the L^∞-normalized counterpart that is to be introduced. This function can be scaled and translated using j and k, and can cover the whole of the domain $[0, 1]$ at each level j.

As shown in Figure 1(a), a box function at scale level j can be expressed as a linear combination of box functions at level $j+1$. This leads to the relation

$$\tilde{\phi}_{j,k}=\tfrac{1}{2}(\tilde{\phi}_{j+1,2k}+\tilde{\phi}_{j+1,2k+1}) \tag{3}$$

The box wavelet, $\tilde{\psi}$, shown in Figure 1(b), can now be introduced. It is defined as

$$\tilde{\psi}_{j,k}=\tfrac{1}{2}(\tilde{\phi}_{j+1,2k}-\tilde{\phi}_{j+1,2k+1}) \tag{4}$$

Combining Equations (3) and (4) leads to the two-scale relations

$$\begin{aligned}\tilde{\phi}_{j+1,2k}&=\tfrac{1}{2}(\tilde{\phi}_{j,k}+\tilde{\psi}_{j,k})\\ \tilde{\phi}_{j+1,2k+1}&=\tfrac{1}{2}(\tilde{\phi}_{j,k}-\tilde{\psi}_{j,k})\end{aligned} \tag{5}$$

An alternative basis would be that of the Haar wavelet, an L^2-normalized counterpart to the box wavelet in Equation (4) that produces an orthogonal wavelet transform. However, the Haar wavelet is the only wavelet both orthogonal and symmetrical. An alternative is to use biorthogonal wavelets, where the orthogonality criterion is relaxed. These allow wavelets to be constructed with

DOI: 10.1002/fld

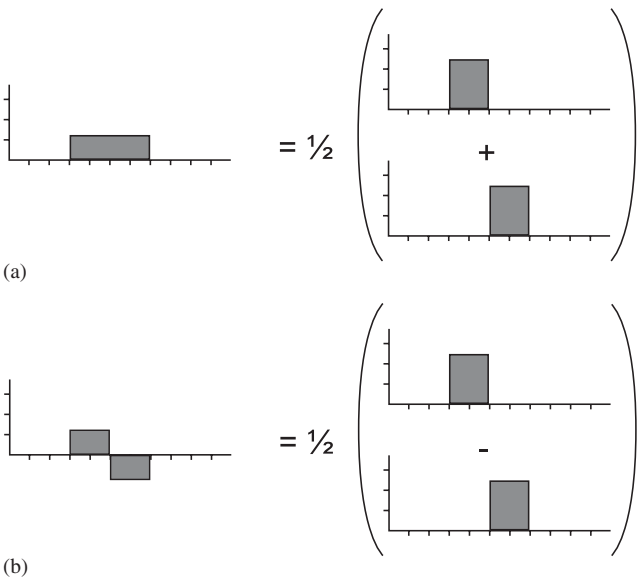

Figure 1. Box function and box wavelet can be constructed from adjacent, high-resolution box functions.

a greater number of vanishing moments while maintaining symmetry (see, for example, [20]). Such a biorthogonal wavelet basis is constructed by introducing the functions ϕ and ψ:

$$\begin{aligned} \phi_{j,k} &= 2^{-j}\tilde{\phi}_{j,k} \\ \psi_{j,k} &= 2^{-j}\tilde{\psi}_{j,k} \end{aligned} \tag{6}$$

Compared with the L^1-normalized box function and box wavelet, ϕ and ψ are L^∞-normalized. As result,

$$\begin{aligned} \int_0^1 \phi_{j,k}\tilde{\phi}_{j,k'}\,\mathrm{d}x &= \delta_{k,k'} \\ \int_0^1 \psi_{j,k}\tilde{\psi}_{j',k'}\,\mathrm{d}x &= \delta_{k,k'}\delta_{j,j'} \end{aligned} \tag{7}$$

where $\delta_{m,n}$ is the Kronecker delta function.

Using these functions introduced in Equation (6) and the biorthogonality shown in Equation (7), an arbitrary function, q, can be projected onto the space of functions piecewise constant over a series of cells, each of size 2^{-j}. This representation, q_j, is given by

$$q_j(x) = \sum_{k=0}^{2^j-1} \int_0^1 q\tilde{\phi}_{j,k}(x')\,\mathrm{d}x'\phi_{j,k}(x) \tag{8}$$

DOI: 10.1002/fld

suggesting approximation coefficients $q_{j,k}$:

$$q_{j,k} = \int_0^1 q(x)\tilde{\phi}_{j,k}(x)\,\mathrm{d}x \tag{9}$$

Similarly, the function q can be projected onto the wavelet basis, $\tilde{\psi}_j$, leading to coefficients known as details, d:

$$d_{j,k} = \int_0^1 q(x)\tilde{\psi}_{j,k}(x)\,\mathrm{d}x \tag{10}$$

For the individual coefficients, two-scale relations similar to Equations (3)–(5) can be found:

$$\begin{aligned} q_{j,k} &= \tfrac{1}{2}(q_{j+1,2k} + q_{j+1,2k+1}) \\ d_{j,k} &= \tfrac{1}{2}(q_{j+1,2k} - q_{j+1,2k+1}) \\ q_{j+1,2k} &= \tfrac{1}{2}(q_{j,k} + d_{j,k}) \\ q_{j+1,2k+1} &= \tfrac{1}{2}(q_{j,k} - d_{j,k}) \end{aligned} \tag{11}$$

Thus combining Equations (9)–(11), and relations (3)–(6), a change of basis can be effected for q_j, using the approximation coefficients $q_{j,k}$ and details, $d_{j,k}$:

$$q_{j+1} = \sum_{k=0}^{2^{j+1}-1} q_{j+1,k}\phi_{j+1,k} = \sum_{k=0}^{2^j-1} q_{j,k}\phi_{j,k} + \sum_{k=0}^{2^j-1} d_{j,k}\psi_{j,k} \tag{12}$$

Therefore a representation of q at finer scales can be obtained by successively adding detail coefficients multiplied by the oscillatory wavelet functions. In the multiscale scheme the function q approximated at level L is first decomposed into an approximation at level 0, the lowest level of discretization, and a series of details. This decomposition is illustrated by

$$\begin{array}{ccccccccccccc} q_L & \to & q_{L-1} & \to & \dots & \to & q_j & \to & \dots & \to & q_1 & \to & q_0 \\ & \searrow & & \searrow & & \searrow & & \searrow & & \searrow & & \searrow & \\ & & d_{L-1} & & \dots & & d_j & & \dots & & d_1 & & d_0 \end{array}$$

The function approximated at level L is decomposed into a coarser approximation at level $L-1$ plus a series of details, d_{L-1}. Coarser approximations are decomposed further into coarser still approximations, with corresponding detail coefficients, until the approximation at level 0 is reached.

While this article only considers one-dimensional problems, it is straightforward to extend the decomposition outlined above to higher dimensions through tensor products of the one-dimensional wavelets. This results in three wavelet functions, corresponding to detail in both grid directions as well as the diagonal.

2.2. Thresholding of details

The detail coefficients combined with the coarse approximation of the decomposed function merely provide an alternative representation, consisting of exactly the same information expressed in a different manner. However, one can show that the magnitudes of the detail coefficients are closely

DOI: 10.1002/fld

related to the local smoothness of function q by rewriting Equation (10), expanding the function $q(x)$ as a Taylor series about point x', the midpoint of the grid cell corresponding to $d_{j,k}$:

$$d_{j,k} = \int_0^1 q(x)\tilde{\psi}_{j,k}(x)\,\mathrm{d}x = \int_0^1 \left(\sum_{m=0}^{\infty} \frac{q^{(m)}(x')}{m!}(x-x')^m \right) \tilde{\psi}_{j,k}\,\mathrm{d}x \tag{13}$$

From Equations (2) and (4),

$$\int_0^1 \tilde{\psi}\,\mathrm{d}x = 0 \tag{14}$$

and, since the wavelet functions are zero away from $x = x'$, the following simplification can be made:

$$d_{j,k} = \int_{S_{j,k}} (x-x')q^{(1)}\tilde{\psi}_{j,k}\,\mathrm{d}x \tag{15}$$

where the inner product integration takes place over the wavelet's support $S_{j,k}$ defined as the non-zero region of $\psi_{j,k}$. Higher derivatives are neglected since $S_{j,k} \ll 1$. Hölder's inequality, a generalization of that of Schwartz, can now be applied:

$$\left| \int f(x)g(x)\,\mathrm{d}x \right| \leqslant \int |f(x)g(x)|\,\mathrm{d}x \leqslant \left(\int |f(x)|^n\,\mathrm{d}x \right)^{1/n} \left(\int |g(x)|^p\,\mathrm{d}x \right)^{1/p} \tag{16}$$

where $1/n + 1/p = 1$. Since the box wavelets, $\tilde{\psi}_{j,k}$ are L^1-normalized, $\|\tilde{\psi}_{j,k}\|_{L^1} = 1$, and taking the cell size to be 2^{-j}, the following inequality holds:

$$\begin{aligned} |d_{j,k}| &\leqslant \|q^{(1)}(x-x')\|_{L^\infty(S_{j,k})} \\ &\leqslant C2^{-j}\|q^{(1)}\|_{L^\infty(S_{j,k})} \end{aligned} \tag{17}$$

where C is a constant. Thus, the magnitude of the detail coefficient is proportional to the gradient of q. Details falling below a predefined value, ε, can therefore be discarded as they do not have a significant effect on the wavelet approximation to the function. By discarding such details, the function q is compressed, in terms of data, and the cell averages are an adapted grid representation of q.

The threshold, ε, is not just an adjustable quantity that must be tuned to achieve an overall accuracy for each different problem; it can be used specifically to set an error bound for the adaptive grid discretization. In order to do this one must first consider an error tolerance, tol, allowable for the solution, and thereby determine the required number of levels of refinement, L, required so that the overall error is within the allowed range; i.e.

$$\|\mathbf{q}_L^n - \tilde{\mathbf{q}}^n\| \leqslant \mathrm{tol} \tag{18}$$

where $\mathbf{q}_L^n$ is the solution to the adaptive scheme at time step n and $\tilde{\mathbf{q}}^n$ is the exact solution at that time. To proceed with some analysis of the error in the scheme it is convenient to separate it into the discretization error and the perturbation error. The discretization error is defined as the error that would be present in what can be called the reference finite-volume computation, i.e. one that used a uniform grid. Thus, if the reference finite-volume scheme solution is $\bar{\mathbf{q}}_L^n$ when discretized

DOI: 10.1002/fld

uniformly to L levels of refinement, the discretization error is given by $\mathbf{e}^n_{L,\text{disc}} = \bar{\mathbf{q}}^n_L - \tilde{\mathbf{q}}^n$. The perturbation error is that which arises from the truncation of the sequence of details and it is given by $\mathbf{e}^n_{L,\text{pert}} = \mathbf{q}^n_L - \bar{\mathbf{q}}^n_L$. The error is therefore required to satisfy

$$\|\mathbf{q}^n_L - \tilde{\mathbf{q}}^n\| \leqslant \|\mathbf{e}^n_{L,\text{disc}}\| + \|\mathbf{e}^n_{L,\text{pert}}\| \leqslant \text{tol} \tag{19}$$

It is assumed that there exists an error estimate for $\mathbf{e}^n_{L,\text{disc}}$, so that $\mathbf{e}^n_{L,\text{disc}} \sim \Delta x^\alpha_L$, where Δx_L is the cell size of the uniform grid at level L, and α is the order of the approximation. From this one could determine L to ensure that $\Delta x^\alpha_L \sim \text{tol}$. If the perturbation error is introduced by discarding details below the so far unspecified threshold ε, the accuracy of the reference finite-volume scheme is then maintained as long as the discretization and perturbation errors are of the same order: $\|\mathbf{e}^n_{L,\text{disc}}\| \sim \|\mathbf{e}^n_{L,\text{pert}}\|$. We may then characterize the required number of levels and the threshold by $L = L(\text{tol}, \alpha)$ and $\varepsilon = \varepsilon(L)$.

Cohen *et al.* [11] defined ε to be a vector, $\boldsymbol{\varepsilon}$, with a different value ε_j for thresholding the details $d_{j,k}$ at each level, given by

$$\varepsilon_j = 2^{(j-L)}\varepsilon \tag{20}$$

with ε a constant parameter. Using Equation (20), these authors show that it is possible to write an estimate for the error at time step n as

$$\|\mathbf{e}^n_{L,\text{pert}}\| \leqslant Cn\varepsilon \tag{21}$$

where C is a constant. The accuracy of the multiscale finite-volume scheme remains that of the reference finite-volume scheme, $\mathbf{e}^n_{L,\text{disc}}$, i.e. of order α, providing ε is sufficiently small that $Cn\varepsilon \sim \Delta x^\alpha_L$.

2.3. Prediction of grid at the next time step

With the scheme described so far, the representation is valid at the time step for which the multiscale transformation with associated threshold is performed but it does not imply that the grid will remain valid for the following time step. A prediction of the grid required at the following time step must be made using the information available at the current time step. Harten [8, 9] introduced a strategy to predict such a grid for hyperbolic conservation laws. He assumed that the speed of propagation is finite and that information concerning the grid moves according to characteristic speeds. In that case each thresholded detail, $d_{j,k}$, (and therefore grid cell) has a range of influence extending one grid cell in all directions assuming that the time step is limited by a Courant number condition, dependent on the cell size and the characteristic speeds. Harten also assumed that discontinuities may develop in the solution and, hence, all the grid cells must be further refined by one level. According to Harten's strategy, the predicted grid at the next time step consists of:

1. All cells in the current grid.
2. Refined cells at a level higher than those containing a significant detail: i.e. a detail greater than the threshold ($|d_{j,k}| \geqslant \varepsilon_j$).
3. Refined cells adjacent to that containing a significant detail.

This is best illustrated by Figure 2, where grid cells that contain significant details are shaded. All such cells are refined, as well as cells adjacent to those containing significant details. The finest grid cells denote the maximum number of refinement levels for this grid.

DOI: 10.1002/fld

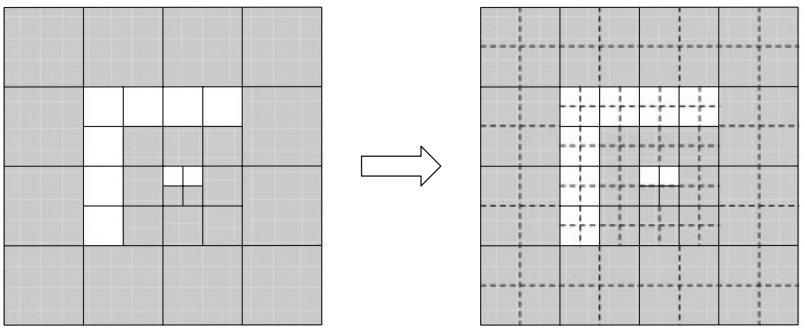

Figure 2. Harten's strategy to predict the grid at the next time step.

For the prediction to be reliable, the grid should contain the significant details on the current time step, n, as well as all of the significant details that would be determined by a multiscale decomposition of the function at time step $n+1$, otherwise unnecessary numerical diffusion would occur with features resolved on a grid that is too coarse, and the error analysis referred to above would be invalid. Harten's strategy has not been proved to guarantee that reliability of prediction, and Cohen *et al.* [11] note that there are pathological situations where the prediction fails. Cohen *et al.* have described an alternative scheme for which the reliability condition has been proved. They found, however, that their scheme was too severe and costly computationally. For their numerical example, they used Harten's prediction strategy. We too have used Harten's scheme for the cases considered below.

2.4. Inverse multiscale transform

Having determined the grid for the next time step it is necessary to perform the inverse multiscale transform to recover the cell-average-based representation necessary for the flux calculation and time integration. This is a straightforward operation using the two-scale recurrence relations in Equation (12). Since the wavelet operators are orthonormal, the inverse matrix for a two-level transformation is simply its transpose. The approximation to the function q at the finest level, L, can thus be recovered by successively applying the inverse transform, as shown in the following schematic diagram

$$\begin{array}{ccccccccccccc} q_0 & \rightarrow & q_1 & \rightarrow & \cdots & \rightarrow & q_j & \rightarrow & \cdots & \rightarrow & q_{L-1} & \rightarrow & q_L \\ & \nearrow & & \nearrow & & \nearrow & & \nearrow & & \nearrow & & \nearrow & \\ d_0 & & d_1 & & \cdots & & d_j & & \cdots & & d_{L-1} & & \end{array}$$

An approximation in the top row is reconstructed using the approximation from the previous level, plus the detail in the bottom row. This process continues until there is either no more detail to add,

DOI: 10.1002/fld

since the approximation is at the highest level, L, or the value of the detail coefficient is zero, in which case there are no further refinements for that cell.

2.5. *Calculation of fluxes and time integration*

Carrying out the inverse multiscale transform results in a series of cell averages at different, threshold-dependent resolutions. Using these cell values the solution at the next time step is calculated. Considering a general conservation law, represented by a vector function, $\mathbf{q}$, we take

$$\mathbf{q}_t + f(\mathbf{q})_x = 0 \tag{22}$$

where details of the particular conservation laws used for $\mathbf{q}$ are given in Section 3. Following the usual finite-volume approach, one can then integrate over a cell, using the divergence theorem, to give

$$\int_V \mathbf{q}_t \, \mathrm{d}v + \int_S f(\mathbf{q}) \, \mathrm{d}s = 0 \tag{23}$$

which, when approximated in the manner of the standard Godunov scheme [21] yields

$$\mathbf{q}_i^{n+1} = \mathbf{q}_i^n - \frac{\Delta t}{\Delta x_i}(f(\mathbf{q}_{i+1/2}^n) - f(\mathbf{q}_{i-1/2}^n)) \tag{24}$$

for each cell, i, where the values of $\mathbf{q}$ at the cell boundaries at time step n are give by $\mathbf{q}_{i+1/2}^n$ and $\mathbf{q}_{i-1/2}^n$. To find these values, we solve a Riemann problem (see, for example, [22, 23]) at the boundary, using the cell averages as the initial conditions. The Riemann problem corresponds to the conservation law, Equation (22), with the initial conditions

$$\mathbf{q} = \begin{cases} \mathbf{q}^{\mathrm{L}}, & x < 0 \\ \mathbf{q}^{\mathrm{R}}, & x > 0 \end{cases} \tag{25}$$

where x is here a coordinate relative to an origin at the cell boundary and superscripts L and R designate the left- and right-hand values, respectively. The solution to this problem is constant along rays of $x/t = \text{constant}$, and the cell-boundary value required is the solution along the ray $x/t = 0$. It is computationally expensive to solve the full Riemann problem, especially since only the solution along the ray $x/t = 0$ is used in the finite-volume computation. Instead, an approximate solution can be obtained using either Roe linearization or the HLLEC method. Details of these methods can be found in [23].

For greater accuracy, higher-order methods can be employed based on reconstructed cell gradients using local cell averages. Using these, methods can be obtained that are formally second-order accurate. As shown by Godunov [21], however, all finite-volume schemes that are linearly second-order accurate and higher produce non-physical oscillations in the solution around discontinuities. To overcome this problem, total variation diminishing schemes have been developed [24] that combine second-order-accurate, piecewise-linear reconstructions of the cell data in areas where the solution is smooth, with first-order, piecewise-constant reconstructions around discontinuities. This switching between first- and second-order schemes is carried out by using slope limiters.

The particular finite-volume scheme used in the present implementation, the MUSCL-Hancock method (see, for example, [23]), consists of the following steps. First, the so-called 'slope-limited'

DOI: 10.1002/fld

gradient, σ, is calculated in each cell i by comparing the gradients obtained from forward and backward differences using adjacent cells:

$$\boldsymbol{\sigma}_i = \text{minmod}((\mathbf{q}_{i+1} - \mathbf{q}_i)/\Delta x_{i+1/2}, (\mathbf{q}_i - \mathbf{q}_{i-1})/\Delta x_{i-1/2}) \tag{26}$$

where $\Delta x_{i+1/2} = (\Delta x_i + \Delta x_{i+1})/2$ and the slope-limiter function, minmod, is given by

$$\text{minmod}(a, b) = \tfrac{1}{2}(\text{sign}(a) + \text{sign}(b)) \min(\text{abs}(a), \text{abs}(b)) \tag{27}$$

This returns the minimum of the two slopes, unless the cell is at a maximum or minimum, in which case the function returns to 0. The limited slope is then used to extrapolate the function $\mathbf{q}_i$ to the cell boundaries, as follows:

$$\begin{aligned} \mathbf{q}_i^{\mathrm{R}} &= \mathbf{q}_i + \frac{\Delta x_i}{2}\boldsymbol{\sigma}_i \\ \mathbf{q}_i^{\mathrm{L}} &= \mathbf{q}_i - \frac{\Delta x_i}{2}\boldsymbol{\sigma}_i \end{aligned} \tag{28}$$

Using Equations (24) and (28), the Hancock predictor step updates the extrapolated cell-boundary values to the midpoint of the time step, $\Delta t/2$:

$$\begin{aligned} \bar{\mathbf{q}}_i^{\mathrm{R}} &= \mathbf{q}_i^{\mathrm{R}} - \frac{\Delta t}{2\Delta x_i}(f(\mathbf{q}_i^{\mathrm{R}}) - f(\mathbf{q}_i^{\mathrm{L}})) \\ \bar{\mathbf{q}}_i^{\mathrm{L}} &= \mathbf{q}_i^{\mathrm{L}} - \frac{\Delta t}{2\Delta x_i}(f(\mathbf{q}_i^{\mathrm{R}}) - f(\mathbf{q}_i^{\mathrm{L}})) \end{aligned} \tag{29}$$

The final update step to the solution at $n+1$ is computed by

$$\mathbf{q}_i^{n+1} = \mathbf{q}_i^n - \frac{\Delta t}{\Delta x_i}(f(\mathbf{q}_{i+1/2}^{\downarrow}) - f(\mathbf{q}_{i-1/2}^{\downarrow})) \tag{30}$$

where $\mathbf{q}_{i+1/2}^{\downarrow}$ is the approximate solution to the Riemann problem at the boundary between cells i and $i+1$, with left- and right-hand input conditions $\bar{\mathbf{q}}_i^{\mathrm{R}}$ and $\bar{\mathbf{q}}_{i+1}^{\mathrm{L}}$, respectively.

The cell averages are then decomposed again into an approximation and a series of detail coefficients and the first stage begin again at the new time step. The adaptive multiscale finite-volume scheme therefore achieves the same order of accuracy as the reference finite-volume scheme on a uniform, high-resolution grid, provided the strategy for predicting the grid for the following time step, outlined in Section 2.3, holds. The suitability of this prediction strategy and the associated claim for the error bound are explored in Section 3, along with the applicability of such a scheme to hydrodynamics problems.

3. APPLICATIONS

In order to determine the effectiveness of the scheme, four different cases have been considered as follows: a dam-break problem, using the shallow water equations; an interacting blast-wave problem; solitary-wave reflection; propagation of a solitary wave over a steep step. These permit comparisons to be made with other published solutions and convergence of the methodology to be investigated. The first two cases are examples of standard hyperbolic problems and the others are based on modelling solitary waves with the Boussinesq equations.

DOI: 10.1002/fld

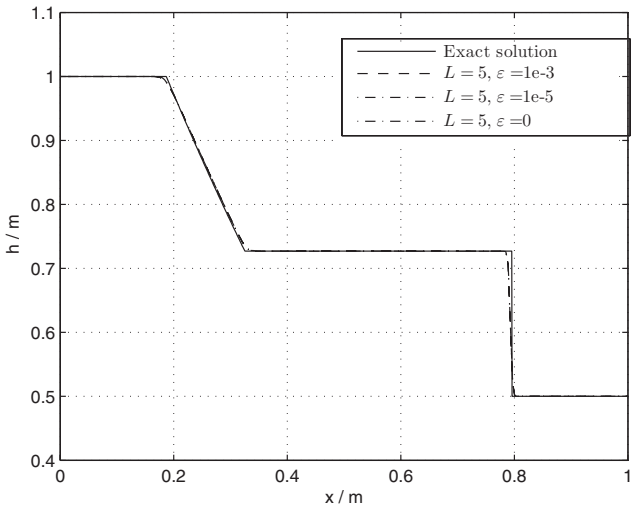

Figure 3. Solution to dam-break problem, comparison with numerical results.

3.1. Hyperbolic problems

3.1.1. Dam-break problem. The dam-break problem is a standard test case for many finite-volume schemes. The governing equations for the problem are the one-dimensional shallow water equations, given by

$$\begin{bmatrix} h \\ hu \end{bmatrix}_t + \begin{bmatrix} hu \\ hu^2 + \frac{1}{2}gh^2 \end{bmatrix}_x = 0 \tag{31}$$

where h is the water height, u is the velocity of the water and g is the acceleration due to gravity. As a problem it is sufficiently simple that the exact solution can be calculated (e.g. [22]) and it is therefore of use for comparison purposes. The initial state consists of two regions of constant height, separated by a discontinuity. The water is initially still, the bed is flat and frictionless and the initial conditions are specified as

$$\begin{aligned} x < 0.5\,\text{m}, &\qquad x \geqslant 0.5\,\text{m} \\ h = 1\,\text{m}, &\qquad h = 0.5\,\text{m} \\ u = 0\,\text{ms}^{-1}, &\qquad u = 0\,\text{ms}^{-1} \end{aligned}$$

The initial discontinuity is thus positioned at $x = 0.5\,\text{m}$, in a domain length of 1 m. The solution to the dam-break problem, as assuming $h > 0\,\text{m}$ throughout, consists of a right-travelling shock wave and a left-travelling rarefaction wave. Figure 3 compares the exact solution, originally found by Stoker [25] with example numerical computations. In these, L, the number of refinement levels is equal to 5, and ε, the threshold parameter defined in Equation (20), is equal to 10^{-3}, 10^{-5} and 0, with this last case corresponding to the uniform grid. It can be seen that the computed numerical results appear to lie over each other. This would suggest that, over the range of ε shown, ε does not

DOI: 10.1002/fld

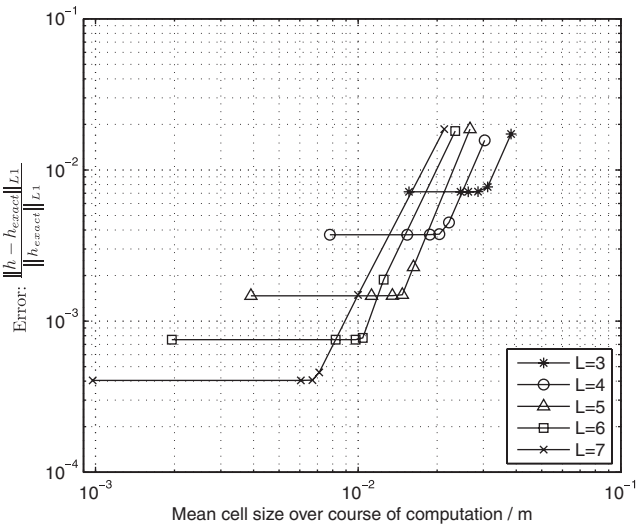

Figure 4. Dam-break problem: normed error against mean cell size.

strongly affect the accuracy of the solution. The relationship between ε and the accuracy is further explored in Figure 4. The error, defined here as the normed proportional difference between the approximate solution and the exact solution, is plotted against the mean number of grid cells per time step over the course of each computation. Results were computed for $L=(3,4,5,6,7)$ with the threshold parameter $\varepsilon=(10^{-1},10^{-2},10^{-3},10^{-4},10^{-5},0)$. Larger values of ε result in less cell refinement and therefore fewer grid cells. For each L line, the left-most point corresponds to $\varepsilon=0$ and the right-most point corresponds to $\varepsilon=10^{-1}$.

Figure 4 shows that, starting from the results with the largest value of ε and the fewest grid cells, there is an initial gradient. As ε decreases, however, and the mean number of grid cells increases, there is a rapid change in the slope. Below a certain value of ε, further reduction has little effect on the accuracy. For example, comparing the case $L=7,\varepsilon=10^{-3}$ with $L=7,\varepsilon=0$, the adaptive grid uses 7 times fewer grid cells for an improvement in accuracy of just 5%. It can be seen that, for the uniform-grid cases, the left-most points on each L line, the gradient is approximately equal to 1 and so the overall scheme exhibits first-order convergence. This is not surprising since most of the solution is flat with just a small region with a large discontinuity, where most of the error arises. In this region the slope limiter adds numerical viscosity to prevent oscillations and the scheme is first-order locally.

Figure 5 shows an example grid in the x–t plane for the case $L=4,\varepsilon=10^{-2}$. Contours of wave height are plotted on top (shown in bold). It can be seen that the right-travelling shock wave maintains a sharp front in the adaptive grid and the grid refines automatically over this and the spreading rarefaction wave.

3.1.2. Interacting blast-wave problem. The interacting blast-wave problem was introduced by Colella and Woodward [19] to test a selection of numerical codes. The governing equations in this case are the Euler equations, given by the following equation, where ρ is the density, u is the

DOI: 10.1002/fld

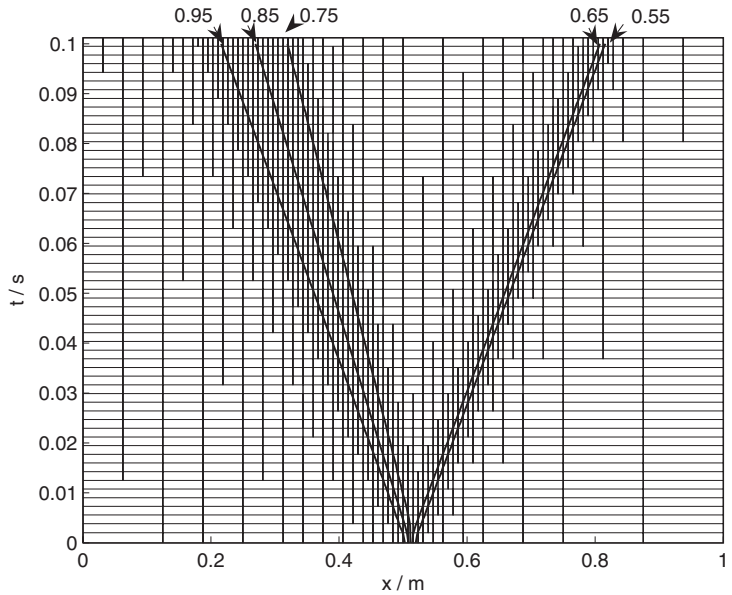

Figure 5. Dam-break problem: x–t representation of adaptive grid for $L=4$, $\varepsilon=10^{-2}$.

velocity, E is the internal energy and p is the pressure:

$$\begin{bmatrix} \rho \\ \rho u \\ E \end{bmatrix}_t + \begin{bmatrix} \rho u \\ \rho u^2 + p \\ (E+p)u \end{bmatrix}_x = 0 \tag{32}$$

The energy is given by

$$E = \frac{p}{\gamma - 1} + \frac{1}{2}\rho u^2 \tag{33}$$

The gas is assumed to be ideal and the ratio of specific heats, γ, equal to 1.4. The Euler equations are used to model a 1 m-long, gas-filled shock tube with sealed ends. Two discontinuities exist in the initial conditions, at $x=0.1$ and 0.9 m. p, ρ and u are as prescribed:

$$\begin{array}{lll} 0 \leqslant x \leqslant 0.1, & 0.1 < x \leqslant 0.9, & 0.9 < x \leqslant 1 \\ p = 1000\,\text{Pa}, & p = 0.01\,\text{Pa}, & p = 100\,\text{Pa} \\ \rho = 1\,\text{kg m}^{-3}, & \rho = 1\,\text{kg m}^{-3}, & \rho = 1\,\text{kg m}^{-3} \\ u = 0\,\text{ms}^{-1}, & u = 0\,\text{ms}^{-1}, & u = 0\,\text{ms}^{-1} \end{array}$$

The pressure ratios in neighbouring regions are 100 000 and 10 000. These lead to very strong shock waves travelling towards the centre of the tube. Rarefaction waves travel away towards the

DOI: 10.1002/fld

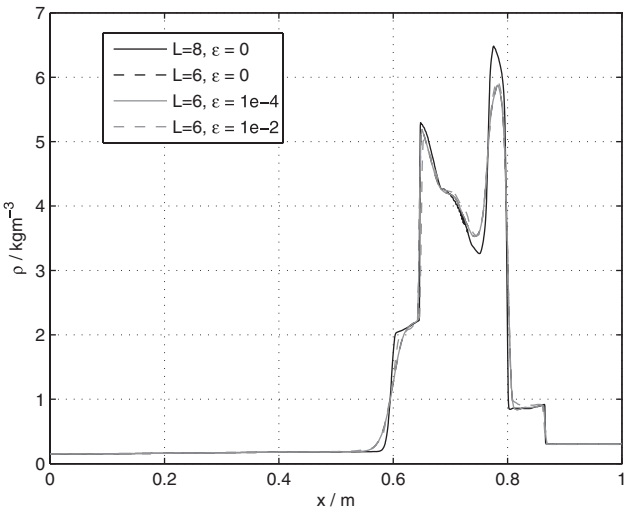

Figure 6. Interacting blast problem: spatial plots at $t=0.038$ s.

end walls initially, before reflecting back towards the tube centre to interact with the other waves. This is a difficult test problem as the wave interactions are complex and there is a large spike in pressure at the point where the two shock waves meet. Riemann solvers based on linearization, such as Roe's method, typically have difficulties with such a feature, predicting a negative density for the Riemann state. There is no analytical solution for this problem but, because of its difficulties, it is a commonly used case for testing codes (for example, [26]). It is used here chiefly because of the complex wave patterns present in the solution, and the contrast in the solution between smooth regions and sharp discontinuities.

The numerical model was run for maximum refinement levels L between 2 and 7, with values of $\varepsilon=(10^{-2}, 10^{-3}, 10^{-4}, 10^{-5}, 10^{-6}, 10^{-7}, 10^{-8}, 10^{-9}, 0)$. Solutions are usually compared at $t=0.038$ s, shortly after the shock waves have interacted. Figure 6 shows the distribution of density along the tube for three cases with $L=6$, $\varepsilon=10^{-2}, 10^{-4}$, compared with the solution on a uniform grid at $L=6$ and 8. The two different threshold values have a significant effect on the solution at $t=0.038$ s. However, even at $L=6$ with $\varepsilon=10^{-2}$, most of the features in the solution are apparent: the steps at $x=0.6$ and 0.8; the region between the two peaks and the peaks themselves. Since there is no exact solution to this problem and, as Colella and Woodward found [19], the order of convergence for the scheme can be at most 1, it was decided to use the solution on the uniform grid at $L=8$ to calculate the errors.

Figure 7 plots the error, defined here as the normed proportional difference between each solution and the uniform-grid solution at $L=8$ for the different maximum refinement levels and threshold values. It can be seen that the adaptive grid cases, where $\varepsilon>0$, produce errors very close to those of the uniform-grid case. For the case $L=7$, the same accuracy is obtained for $\varepsilon=10^{-3}$ as for $\varepsilon=0$, suggesting that the error bound of Equations (19) and (21) holds. For $\varepsilon=10^{-3}$, a quarter of the number of grid cells is used over the computation, thus taking a quarter of the time.

These results can be compared favourably with those of Toro [26]. Figure 8 shows the density, velocity, pressure and internal energy for the case $L=8$, $\varepsilon=10^{-4}$ at $t=0.028$ s. Over the course of

DOI: 10.1002/fld

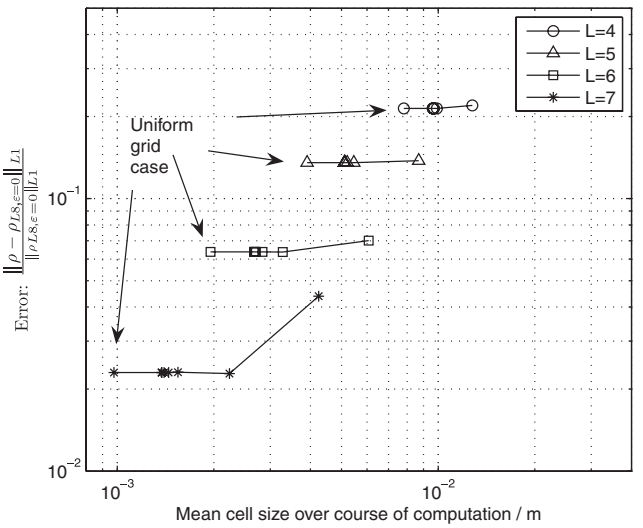

Figure 7. Interacting blast problem: normed error against mean cell size.

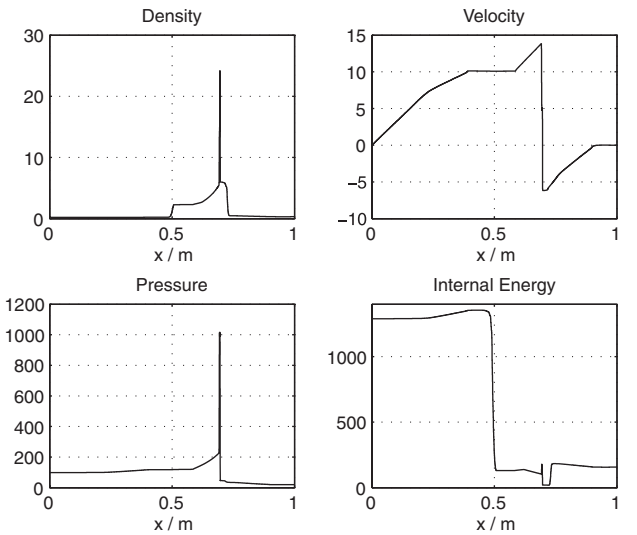

Figure 8. Interacting blast problem: density, velocity, pressure and internal energy at $t = 0.028\,\mathrm{s}$ for $L = 8$, $\varepsilon = 10^{-4}$.

this computation, an average of 658 cells were used per time step, compared with 3000 in [26]. The density spike of approximately $25\,\mathrm{kg\,m^{-3}}$ in Figure 8 is sharper and higher than that of Toro [26], though lower than that of Colella and Woodward's [19] reference piecewise-parabolic method using 4000 grid cells; they obtained a density spike of approximately $28\,\mathrm{kg\,m^{-3}}$.

DOI: 10.1002/fld

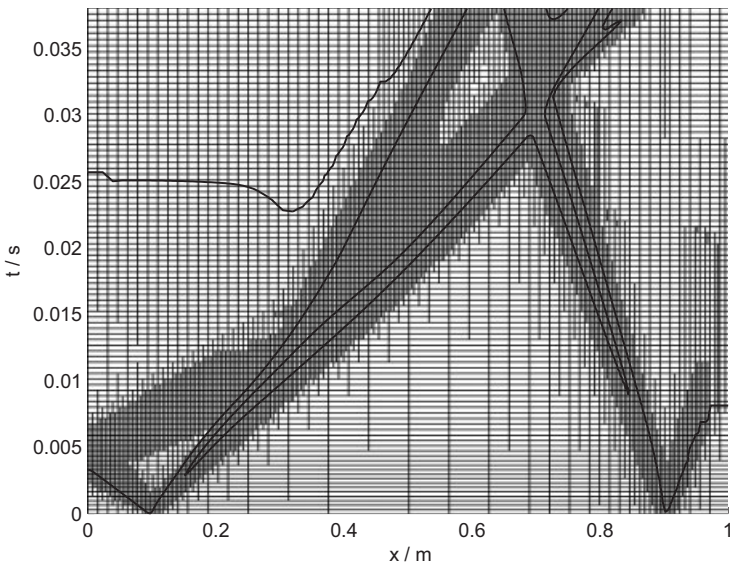

Figure 9. Interacting blast problem: $L=5$, $\varepsilon=10^{-2}$, grid with overlain density contour plot.

Figure 9 plots contours of the density in the x–t plane over a representation of the adaptive grid over the course of the computation. It can be seen that the adaptive grid is effective at tracking the solution, with the grid refining automatically over the shocks and rarefactions.

3.2. Solitary-wave test cases using Boussinesq equations

The following test cases extend application of the adaptive multiscale one-dimensional scheme to the Boussinesq equations. These equations contain source terms, and feature a correction step where an elliptic equation is solved. In this respect the problem is similar to the Euler equations for incompressible flow where, in order to calculate the pressure, Poisson's equation must be solved. The specific Boussinesq equation set used is a finite-volume formulation of Madsen and Sørensen's Boussinesq equations [27]. The equations are described briefly below and further details of the derivation can be found in [28]. The hyperbolic equations used in the finite-volume stage are expressed as follows, in terms of variables defined below:

$$\zeta_t + P_x = 0 \tag{34}$$

$$\tilde{P}_t + \left[\frac{P^2}{d} + \frac{1}{2}g(\zeta^2 + 2\zeta h)\right]_x = g\zeta h_x + Bgh^3\zeta_{xxx} + 2Bgh^2 h_x \zeta_{xx} \tag{35}$$

The water level, h, now represents the depth to the mean water line.[‡] ζ represents the surface elevation above the mean water line and P represents the momentum, given by $P=u(\zeta+h)$. As before, u is the velocity. The constant B originates from one of the coefficients of the Padé approximants

[‡]As one of the example test cases involves a non-uniform bathymetry, h cannot be used to represent the total water height, unlike in the dam-break problem.

DOI: 10.1002/fld

which model the dispersion relationship: its value is taken here to be $\frac{1}{15}$. $\tilde{P}$ is a 'transformed' version of P, created by transferring the time–space cross-derivatives from Madsen and Sørensen's formulation to the left-hand side of the equation. The transformation, A, is defined by

$$\begin{aligned}\tilde{P} &= P - \left(B + \frac{1}{3}\right) h^2 P_{xx} - \frac{1}{3} h h_x P_x \\ &= \left(I - \left(B + \frac{1}{3}\right) h^2 \frac{\partial^2}{\partial x^2} - \frac{1}{3} h h_x \frac{\partial}{\partial x}\right) P \\ &= AP \end{aligned} \tag{36}$$

To solve the equations, the variables, ζ and P, are combined in the vector $\mathbf{q}$:

$$\mathbf{q} = \begin{bmatrix} \zeta \\ P \end{bmatrix}, \quad \tilde{\mathbf{q}} = \begin{bmatrix} \zeta \\ \tilde{P} \end{bmatrix}$$

and the source term vector is constructed using the right-hand side terms of Equations (34) and (35):

$$\mathbf{S} = \begin{bmatrix} 0 \\ g\zeta h_x + Bgh^3 \zeta_{xxx} + 2Bgh^2 h_x \zeta_{xx} \end{bmatrix} \tag{37}$$

For second-order accuracy, a second-order Runge–Kutta scheme, evaluating in cell i at time step n, is used to give a four-stage scheme:

1. $\tilde{\mathbf{q}}_i^{n+1/2} = \tilde{\mathbf{q}}_i^n - \frac{\Delta t}{2\Delta x}(f(\mathbf{q}_{i+1/2}^n) - f(\mathbf{q}_{i-1/2}^n)) + \frac{\Delta t}{2} S_i^n$
2. $P^{n+1/2} = A^{-1} \tilde{P}^{n+1/2}$
3. $\tilde{\mathbf{q}}_i^{n+1} = \tilde{\mathbf{q}}_i^n - \frac{\Delta t}{\Delta x}(f(\mathbf{q}_{i+1/2}^{n+1/2}) - f(\mathbf{q}_{i-1/2}^{n+1/2})) + \Delta t S_i^{n+1/2}$
4. $P^{n+1} = A^{-1} \tilde{P}^{n+1}$

To calculate the second- and third-order derivatives that occur in the source terms $\mathbf{S}$ and in the operator A in the elliptic correction (stages 2 and 4 above), second-order explicit finite difference approximations suitable for a non-uniform grid were used, determined by matching Taylor series coefficients to eliminate sufficient truncation error for the desired order of accuracy. Evaluation of the elliptic correction stages involves solution of a large system of simultaneous equations.

3.2.1. Solitary-wave reflection. In this test case, solitary waves of heights 0.10, 0.20, 0.30 and 0.40 m propagate in water at a constant depth of $h = 1$ m until the waves reach a wall, from which they are reflected back. The domain length is 30 m and the solitary waves are initially centred at $x = 10$ m. A diagram of the initial set-up is shown in Figure 10. The initial height distribution, as given by Laitone [29], is

$$\frac{\zeta_0(x)}{h} = \frac{a_0}{h} \operatorname{sech}(\alpha X)^2 - \frac{3}{4}\left(\frac{a_0}{h}\right)^2 \operatorname{sech}(\alpha X)^2 (1 - \operatorname{sech}(\alpha X)^2) \tag{38}$$

where a_0 is the prescribed initial wave amplitude and

$$\alpha X = \frac{x}{h}\left(\frac{3a_0}{4h}\right)^{1/2}\left(1 - \frac{5a_0}{8h}\right) \tag{39}$$

DOI: 10.1002/fld

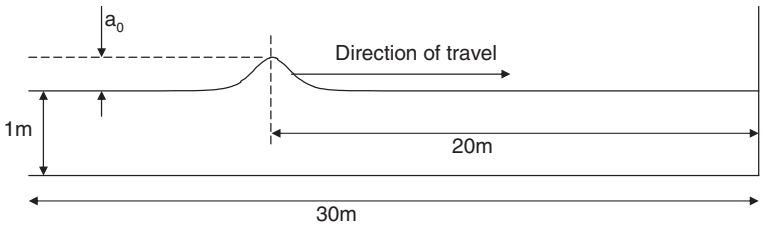

Figure 10. Solitary-wave reflection case: initial wave profile.

The initial velocity is given by

$$\frac{u(\infty)}{\sqrt{gh}} = 1 + \frac{1}{2}\frac{a_0}{h} - \frac{3}{20}\left(\frac{a_0}{h}\right)^2 \tag{40}$$

Applying the adaptive grid, instability was encountered for the cases $L=8$, 9, $\varepsilon>0$ and for $L=7, \varepsilon>10^{-4}$ (Figure 11). For the cases presented here, a Courant number of $C=0.6$ has been used; at these higher resolutions the scheme was unstable even with a Courant number of 0.06. The effect of even smaller time steps was explored on smaller test problems using a reduced spatial domain (for reasons of speed) and the scheme was unstable even for $C=0.006$ at these resolutions. The scheme nevertheless remained stable for the uniform-grid case. The cause of the instability was traced to the third derivative in the source term, shown in Equation (37). Replacing the original five-point centred finite difference expression with a seven-point expression was also unsuccessful. Stability problems for dispersive waves were also encountered in finite difference schemes by Garcia-Archilla [30] and by Saucez *et al.* [31] for the Korteweg–de Vries equation; in these cases the instability was caused by the discretization of the third derivative. It is not possible to implement a stable, implicit finite difference stage for the source terms as S is not a function of P—the surface elevation and momentum are decoupled. Garcia-Archilla [30] and Garcia-Archilla and Sanz-Serna [32] present a finite difference scheme to calculate the third derivative for the Korteweg–de Vries equation on a non-uniform grid. However, their scheme is only suitable for grids having periodic boundary conditions and with an odd number of cells; on grids with an even number of cells the truncation errors do not decrease with cell size. This is not appropriate for the adaptive scheme considered here. It was decided therefore to consider only the stable results and hence $\varepsilon=10^{-5}$ was used.

Figure 12 plots the run-up at the wall, R, divided by the initial amplitude against normalized initial amplitude. The line $R/a_0=2$ represents linear superposition. A non-linear interaction component can clearly be seen as the ratio R/a_0 increases with amplitude. We first consider the results from the uniform-grid cases. Richardson extrapolation was applied to the calculated results, showing that convergence had been obtained. Also plotted on this graph are the results for $L=5$, 6 and 7 with $\varepsilon=10^{-5}$, for where computations the scheme was stable. The run-up values calculated from these adaptive computations approach those for the uniform grid.

3.2.2. Propagation of a solitary wave over a steep step. It was found by Madsen and Mei [33] that when a solitary wave travels over a step into shallower water, fission can occur. The solitary wave breaks down, leaving a number of solitary waves, usually with a small oscillatory tail. Both Tappert and Zabusky [34] and Johnson [35] use the Korteweg–de Vries equation to show that the

DOI: 10.1002/fld

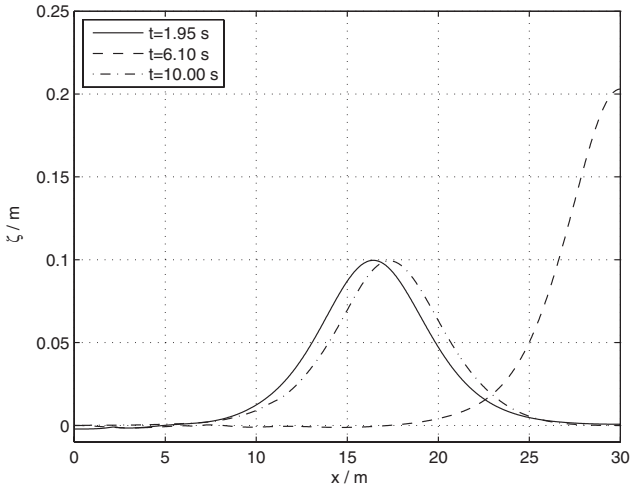

Figure 11. Example of solitary reflection at wall for $L=7$, $\varepsilon=10^{-3}$ for $a_0/h=0.1$.

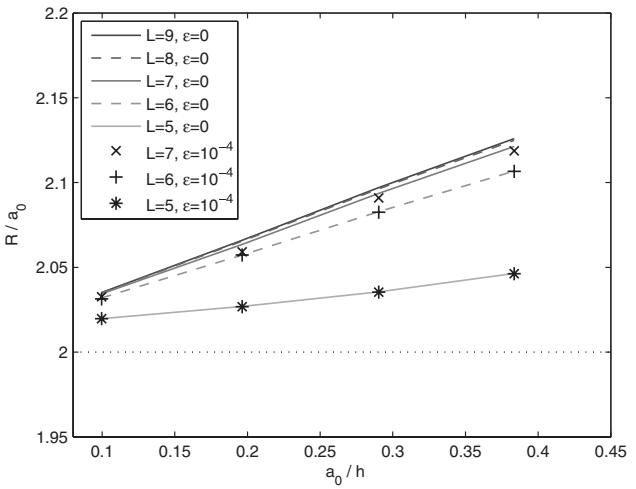

Figure 12. Run-up at wall for various levels of refinement. The dotted line at $R/a_0=2$ represents linear superposition. The uniform grid ($\varepsilon=0$) and stable adaptive grid are also shown ($\varepsilon>0$).

number of waves produced depends on the ratio of depths, and they also give an expression for the amplitudes of the fission solitary waves, in the form of amplification factors, A_m. The number of solitary waves formed, p, is found from

$$\frac{h_1}{h_0}=\left(\frac{p(p+1)}{2}\right)^{-4/9} \tag{41}$$

DOI: 10.1002/fld

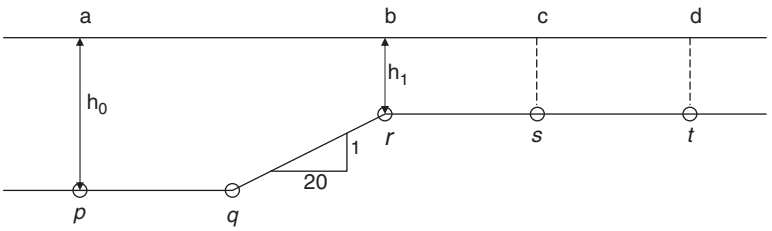

Figure 13. Madsen and Mei experiment—gauge positions and bathymetry. Coordinates of positions p, q, r, s and t in text.

where h_1/h_0 is the ratio of water depths, in this case 0.5. To predict the amplitudes of the fission solitary waves, the amplification factors are given by

$$A_m = \frac{2a_0(\Delta+m)^2}{p(p+1)} \tag{42}$$

where $\Delta = 1+p-N$ and N is the largest integer satisfying $N \leqslant p+1$. The Δ term allows for the fact that Equation (41) will not typically produce an integer number of solitary waves; in these cases the oscillatory tail is formed. For $h_1/h_0 = 0.5$, three solitary waves are formed, with amplification factors $A_1 = 1.722$, $A_2 = 0.660$ and $A_3 = 0.100$.

Madsen and Mei [33] performed a series of experiments exploring this phenomenon. The bathymetry used in these experiments is shown in Figure 13, with positions relative to an origin to the left of the region shown. The coordinates (in metres) of the gauge positions and slope discontinuity locations, p, q, r, s and t are $(3, 0)$, $(3.4064, 0)$, $(4.1684, 0.009144)$, $(5.0574, 0.009144)$ and $(5.921, 0.009144)$, respectively; in the experiments, imperial measurements were used, with an initial water depth, h_0, of 3 in (0.0762 m).

The initial amplitude was taken as $\zeta_0/h_0 = 0.12$. From Equations (41) and (42), this gives relative amplitudes after fission of $\zeta_1/h_0 = 0.207$, $\zeta_2/h_0 = 0.0792$ and $\zeta_3/h_0 = 0.0117$, which compare favourably with results of the Korteweg–de Vries equations computed from a numerical model in [33], but not with the experimental results. The solitary-wave experiments of Madsen and Mei [33] are, therefore, suitable for comparison with the results from the scheme described in the present paper, as there exist physical results and an analytical solution with which to compare, though the latter is for the Korteweg–de Vries equation rather than the Boussinesq equations. The case was run for L, the number of refinement levels, equal to 5, 6, 7, 8, 9 and 10 with ε, the threshold parameter, set to $10^{-1}, 10^{-2}, 10^{-3}, 10^{-5}$ and 0.

Instability was encountered for the cases $L = 9, \varepsilon = 10^{-1}, 10^{-2}, 10^{-3}$ and for all values of $\varepsilon > 0$ at $L = 10$ and above. Just as for the solitary-wave reflection case in Section 3.2.1, the instability was caused by the third derivative discretization on the non-uniform grid. It was decided therefore to consider only the stable results and, hence, for comparison with experimental data, $\varepsilon = 10^{-5}$ was used.

Three time histories are plotted in Figure 14 for these parameters, showing the elevation at three of the gauge positions used by Madsen and Mei [33]. At gauge position 'b' the solitary wave had begun to deform and is no longer symmetrical. Owing to shoaling, the amplitude is larger than the initial value of $\zeta_0/h_0 = 0.12$. At gauge position 'c' a point of inflection is clear as the largest of the fission waves begins to separate and at gauge position 'd' the separation into fission waves

DOI: 10.1002/fld

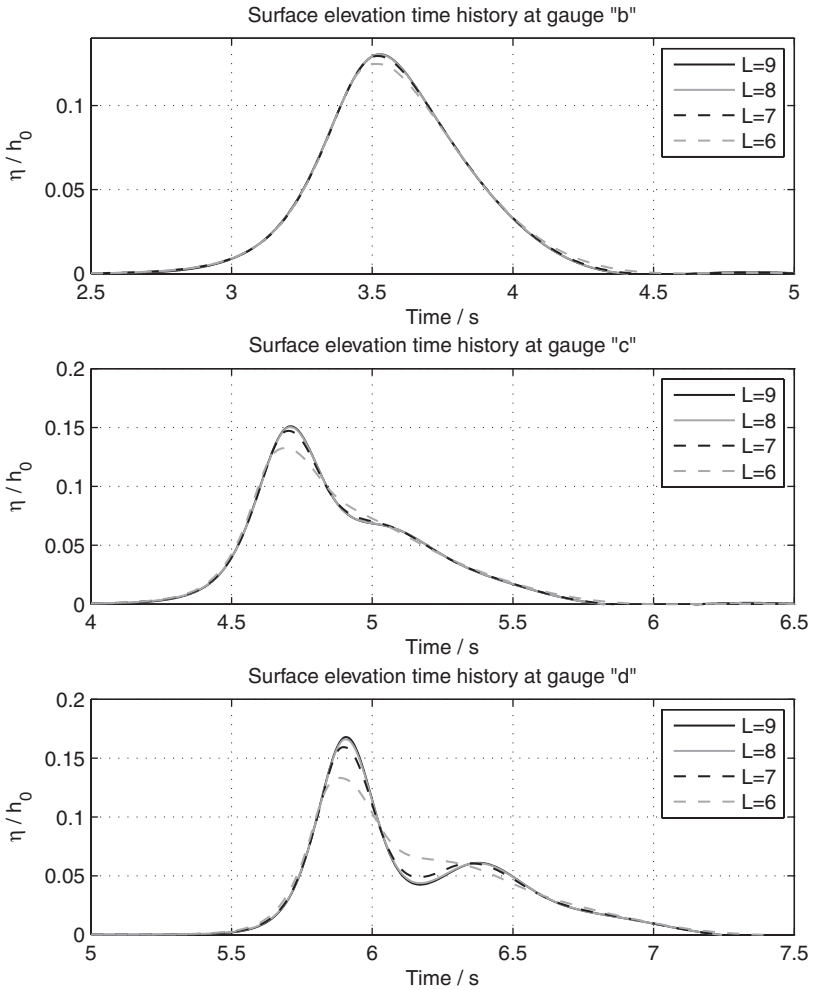

Figure 14. Madsen and Mei case: surface elevation time histories.

is even more apparent. For all but the $L=6$ case, the solutions resolve the wave separation with some clarity. The results for $L=9$ and 8 overlie each other for the first two gauges and remain closed for gauge 'd', suggesting a degree of convergence.

Table I gives the amplitudes of the largest fission solitary waves at gauge 'd' for four different values of L.

Undertaking Richardson extrapolation using the results for $L=8$ and 9, with $\varepsilon=10^{-5}$, the converged amplitude is 0.1685. Using this converged value, Figure 15 plots the error at gauge 'd' for the stable cases studied. As before, the adaptive grid gives results as accurate as those on the uniform grid, but using far fewer grid cells; for the case of $L=8$, the same accuracy is obtained using one-seventh the number of grid cells.

DOI: 10.1002/fld

Table I. Computed amplitudes of largest fission solitary waves at gauge 'd' for differing maximum resolutions.

L	ζ_1/h_0
6	0.1333
7	0.1593
8	0.1659
9	0.1678

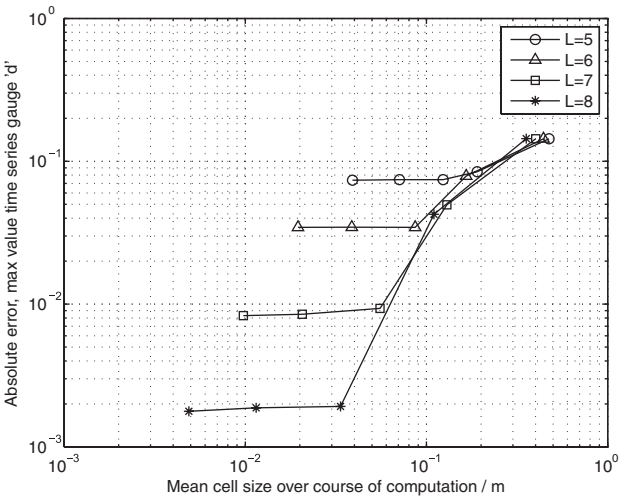

Figure 15. Madsen and Mei case: error at gauge 'd' against mean cell size (stable cases only).

The converged value of the amplitude at gauge 'd' is significantly below the analytically determined value above, 0.207. However, since the latter has been obtained from the solution of the Korteweg–de Vries equation, it is unsurprising that a discrepancy such as this might be found. In particular, one can note an important difference between the models: the Korteweg–de Vries equation admits solutions travelling in just one direction, whereas the Boussinesq equations can admit both left- and right-travelling waves and as such are able to model the reflected wave from the step. Peregrine [36] shows that the reflected wave is of almost constant height, with a length approximately equal to twice the horizontally projected length of the slope, 1.52 m in this case. Peregrine also gives an expression for calculating the reflected wave height, ζ_{ref}, in terms of the bed slope, α and the initial amplitude ζ_0 relative to the depth h_0:

$$\frac{\zeta_{\text{ref}}}{h_0} = \frac{1}{2}\alpha\left(\frac{1}{3}\frac{\zeta_0}{h_0}\right)^{1/2} \tag{43}$$

For the case of $\alpha = \frac{1}{20}$ and $\zeta_0/h_0 = 0.12$, this equation gives $\zeta_{\text{ref}}/h_0 = 0.005$. As can be seen in the spatial profile in Figure 16, for the computed case $L = 9, \varepsilon = 10^{-5}$, the relative height of the reflected wave varied across its length between 0.005 and 0.006 and the length of the reflected wave was approximately 1.5 m. This could feasibly account for at least part of the difference in

DOI: 10.1002/fld

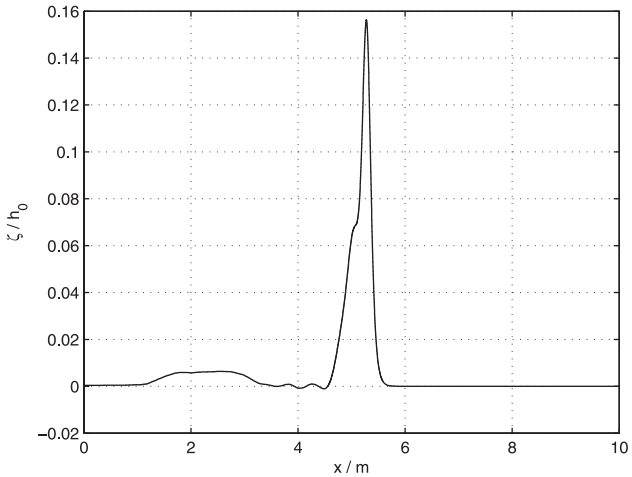

Figure 16. Madsen and Mei case: spatial plot at $t=5$ s showing wave reflected from step ($L=9$, $\varepsilon=10^{-5}$).

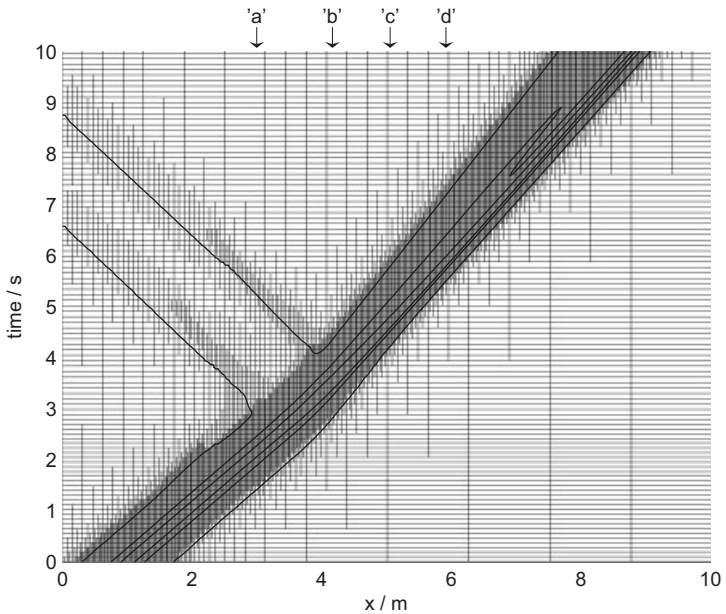

Figure 17. Madsen and Mei case: adaptive grid ($L=6, \varepsilon=10^{-3}$) with overlain contour plot of ζ/h_0. Contours shown are 0.0025, 0.0525 and 0.1025. Positions of gauges 'a', 'b' 'c' and 'd' are shown for reference.

height between the Korteweg–de Vries analytical solutions and the computed results presented here.

As Madsen and Mei [33] note, for the water depth considered here, friction has a significant effect. To account for the friction in comparing their own computed results with the experimental data, Madsen and Mei make use of the experimental results of Ippen *et al.* [37] and an empirical

DOI: 10.1002/fld

formula for viscous wave attenuation given therein. Using this, Madsen and Mei estimate the undamped relative wave height to be approximately 0.16, in good agreement with results presented here, and a considerable improvement on the Korteweg–de Vries-derived analytical results.

An example grid for this case is shown in Figure 17, where the positions of gauges 'a', 'b', 'c' and 'd' are marked. It can be seen the grid adapts smoothly to this case, resolving the wave reflected from the step as well as the transmitted waves. Contours of wave elevation are overlain, indicating how the grid has adapted in regimes of rapid change.

4. CONCLUSIONS

The adaptive finite-volume scheme described in Section 2 has been investigated using four cases presented in Section 3. In the first two cases, the dam break using the shallow water equations and the interacting blast-wave problem using the Euler equations, the accuracy of the scheme was explored for a range of different values of L, the number of refinement levels, and, ε, the threshold parameter. It was seen that an accuracy equivalent to that of the uniform grid could be obtained using the adaptive grid, thereby using far fewer grid cells. In the dam-break problem, for some combinations the uniform-grid accuracy could be obtained using 7 times fewer cells. For the interacting blast-wave problem, the factor was 4. We have thus demonstrated that, for these problems, the adaptive multiscale scheme, as originally presented by Cohen *et al.* [11] and detailed further by Müller [15], can produce accurate and reliable results using fewer grid cells and therefore taking much less time than for a uniform grid at the finest resolution.

Results were also presented for the adaptive solution of a finite-volume formulation of the Madsen and Sørensen Boussinesq equations. The cases considered were a reflection of a solitary wave by a wall, and propagation of a solitary wave by a step. These have highly localized flow features, which means that large regions can be modelled at low resolution and can therefore take advantage of the adaptive multiscale scheme. Again it was found that results converged onto those obtained from a uniform grid, but using far fewer cells. In these cases, however, instabilities were encountered when very fine resolutions were adopted. These appear to be associated with the treatment of the third spatial derivative in Equation (37) when using a non-uniform grid. Instabilities did not arise in the uniform-grid implementation. We can conclude that there are potential limitations in the application of the present approach to the particular form of Boussinesq equations used here. No such difficulties have been identified in using the proposed method for solving the shallow water or Euler equations in one spatial dimension, and it seems reasonable to infer that such problems in two dimensions could also be satisfactorily resolved using this wavelet-based approach.

Finally, we observe that the finite-volume formulation of the Boussinesq equations involved the solution, at each time step, of a large system of matrix equations, analogous to the Poisson equation for pressure used to model incompressible flow. The solution of these equations did not increase the computational burden significantly, and this, therefore, suggests that the simulation of wave motion and diffraction using the incompressible Euler equations in two dimensions is feasible using the present scheme.

ACKNOWLEDGEMENT

The first author is supported through an EPSRC studentship.

DOI: 10.1002/fld

REFERENCES

1. Craik ADD. The origins of water wave theory. *Annual Review of Fluid Mechanics* 2000; **36**:1–28.
2. Cohen A, Dahmen W, DeVore R. Adaptive wavelet techniques in numerical simulation. In *Encyclopedia of Computational Mechanics*, Stein E, de Borst R, Hughes TJ (eds). Wiley: New York, 2004.
3. Dahmen W. Wavelet and multiscale methods for operator equations. *Acta Numerica* 1997; **6**:57–228.
4. Dahmen W. Wavelet methods for PDEs—some recent developments. *Journal of Computational and Applied Mathematics* 2001; **128**:133–185.
5. Dahlke S, Dahmen W, DeVore R. Stable multiscale bases and local error estimation for elliptic problems. *Applied Numerical Mathematics* 1997; **23**:21–48.
6. Amaratunga K, Williams JR, Qian S, Weiss J. Wavelet-Galerkin solutions for one-dimensional partial differential equations. *International Journal for Numerical Methods in Engineering* 1994; **37**:2703–2716.
7. Bertoluzza S. An adaptive collocation method based on interpolating wavelets. In *Multiscale Wavelet Methods for PDEs*, Dahmen W, Kurdila AJ, Oswald P (eds). Academic Press: London, 1997.
8. Harten A. Multiresolution schemes for shock computations. *Journal of Computational Physics* 1994; **115**:319–339.
9. Harten A. Multiresolution algorithms for the numerical solution of hyperbolic conservation laws. *Communications on Pure and Applied Mathematics* 1995; **48**:1305–1342.
10. Bihari B, Harten A. Multiresolution schemes for the numerical solution of 2-D conservation laws. *SIAM Journal on Scientific Computing* 1997; **18**:315–354.
11. Cohen A, Kaber SM, Müller S, Postel M. Fully adaptive multiresolution finite volume schemes for conservation laws. *Mathematics of Computation* 2001; **72**:183–225.
12. Cohen A, Dyn N, Kaber SM, Postel M. Multiresolution schemes on triangles for scalar conservation laws. *Journal of Computational Physics* 2000; **161**:264–286.
13. Bramkamp F, Lamby P, Müller S. An adaptive multiscale finite volume solver for unsteady and steady state flow computations. *Journal of Computational Physics* 2004; **197**:460–490.
14. Andreae S, Ballmann J, Müller S, Voß A. Dynamics of collapsing bubbles near walls. *Hyperbolic Problems*: *Proceedings of the Ninth International Conference on Hyperbolic Problems*, Caltech, Pasadena, March 25–29, 2002, You TY, Tadmor E (eds). Springer, GmbH & Co. K: Berlin, Heidelberg 2003.
15. Müller S. *Adaptive Multiscale Schemes for Conservation Laws*. Lecture Notes in Computational Science & Engineering. Springer, GmbH & Co. K: Berlin, Heidelberg, 2003.
16. Greaves DM, Borthwick AGL. On the use of adaptive hierarchical meshes for numerical simulation of separated flows. *International Journal for Numerical Methods in Fluids* 1998; **26**:303–322.
17. Ham FE, Lien FS, Strong AB. A cartesian grid method with transient anisotropic adaptation. *Journal of Computational Physics* 2002; **179**:469–494.
18. Wang JP, Borthwick AGL, Eatock Taylor R. Finite-volume-type VOF method on dynamically adaptive quadtree grids. *International Journal for Numerical Methods in Fluids* 2004; **45**:485–508.
19. Colella P, Woodward PR. The piecewise parabolic method (PPM) for gas-dynamical simulations. *Journal of Computational Physics* 1984; **54**:174–201.
20. Mallat S. *A Wavelet Tour of Signal Processing* (2nd edn). Academic Press: New York, 1999.
21. Godunov SK. A finite difference method for the numerical computation and discontinuous solutions of the equations of fluid dynamics. *Matematicheskii Sbornik* 1959; **47**:271–306.
22. Leveque RJ. *Finite Volume Methods for Hyperbolic Problems*. Cambridge Texts in Applied Mathematics. Cambridge University Press: Cambridge, 2002.
23. Toro EF. *Riemann Solvers and Numerical Methods for Fluid Dynamics—a Practical Introduction*. Springer, GmbH & Co. K: Berlin, Heidelberg, 1999.
24. Harten A. High resolution schemes for hyperbolic conservation laws. *Journal of Computational Physics* 1983; **49**:357–393.
25. Stoker JJ. *Water Waves*: *The Mathematical Theory with Applications*. Interscience Publishers: New York, 1957.
26. Toro EF. A linearized Riemann solver for the time-dependent Euler equations of gas dynamics. *Proceedings of the Royal Society of London A—Mathematical and Physical Sciences* 1991; **434**:683–693.
27. Madsen PR, Sørensen OR. A new form of the Boussinesq equations with improved linear dispersion characteristics. Part 2. A slowly varying bathymetry. *Coastal Engineering* 1992; **18**:183–204.
28. Borthwick AGL, Ford M, Weston BP, Taylor PH, Stansby PK. Solitary wave transformation, breaking and run-up at a beach. *ICE Proceedings*: *Maritime Engineering* 2006; **159**:97–105.
29. Laitone EV. The 2nd approximation to cnoidal and solitary waves. *Journal of Fluid Mechanics* 1960; **9**:431–443.

DOI: 10.1002/fld

30. Garcia-Archilla B. A supraconvergent scheme for the Korteweg–de Vries equation. *Numerische Mathematik* 1992; **61**:291–310.
31. Saucez P, Wouwer AV, Schiesser WE, Zegeling P. Method of lines study of nonlinear dispersive waves. *Journal of Computational and Applied Mathematics* 2004; **168**:413–423.
32. Garcia-Archilla B, Sanz-Serna JM. A finite difference formula for the discretization of d^3/dx^3 on nonuniform grids. *Mathematics of Computation* 1991; **57**:239–257.
33. Madsen OS, Mei CC. The transformation of a solitary wave over an uneven bottom. *Journal of Fluid Mechanics* 1969; **39**:781–791.
34. Tappert FD, Zabusky NJ. Gradient-induced fission of solitons. *Physical Review Letters* 1971; **27**:1774–1776.
35. Johnson RS. On the development of a solitary wave moving over an uneven bottom. *Proceedings of the Cambridge Philosophical Society* 1973; **73**:183–203.
36. Peregrine DH. Long waves on a beach. *Journal of Fluid Mechanics* 1967; **27**:815–827.
37. Ippen AT, Kulin G, Raza MA. M.I.T. Hydrodynamics Laboratory Technical Report No. 16. *Technical Report*, M.I.T., 1955.

DOI: 10.1002/fld